AD_____

Award Number: DAMD17-02-1-0326

TITLE: Electrical Impedance Tomography of Breast Cancer

PRINCIPAL INVESTIGATOR: L. Tugan Muftuler, Ph.D.

CONTRACTING ORGANIZATION: University of California, Irvine
                           Irvine, California 92697-1875

REPORT DATE: June 2004

TYPE OF REPORT: Annual

PREPARED FOR: U.S. Army Medical Research and Materiel Command
               Fort Detrick, Maryland 21702-5012

DISTRIBUTION STATEMENT: Approved for Public Release;
                        Distribution Unlimited

The views, opinions and/or findings contained in this report are
those of the author(s) and should not be construed as an official
Department of the Army position, policy or decision unless so
designated by other documentation.

20041118 076

REPORT DOCUMENTATION PAGE		Form Approved OMB No. 074-0188

Public reporting burden for this collection of information is estimated to average 1 hour per response, including the time for reviewing instructions, searching existing data sources, gathering and maintaining the data needed, and completing and reviewing this collection of information. Send comments regarding this burden estimate or any other aspect of this collection of information, including suggestions for reducing this burden to Washington Headquarters Services, Directorate for Information Operations and Reports, 1215 Jefferson Davis Highway, Suite 1204, Arlington, VA 22202-4302, and to the Office of Management and Budget, Paperwork Reduction Project (0704-0188), Washington, DC 20503

1. AGENCY USE ONLY (Leave blank)	2. REPORT DATE June 2004	3. REPORT TYPE AND DATES COVERED Annual (6 May 2003 - 5 May 2004)	

4. TITLE AND SUBTITLE Electrical Impedance Tomography of Breast Cancer	5. FUNDING NUMBERS DAMD17-02-1-0326

6. AUTHOR(S)
L. Tugan Muftuler, Ph.D.

7. PERFORMING ORGANIZATION NAME(S) AND ADDRESS(ES) University of California, Irvine Irvine, California 92697-1875 E-Mail: muftuler@uci.edu	8. PERFORMING ORGANIZATION REPORT NUMBER

9. SPONSORING / MONITORING AGENCY NAME(S) AND ADDRESS(ES) U.S. Army Medical Research and Materiel Command Fort Detrick, Maryland 21702-5012	10. SPONSORING / MONITORING AGENCY REPORT NUMBER

11. SUPPLEMENTARY NOTES
Original contains color plates: All DTIC reproductions will be in black and white.

12a. DISTRIBUTION / AVAILABILITY STATEMENT Approved for Public Release; Distribution Unlimited	12b. DISTRIBUTION CODE

13. ABSTRACT (Maximum 200 Words)

In screening of breast cancer, once abnormalities or lesions are discovered by the X-ray mammogram, generally, other imaging techniques are needed as an adjunct to diagnose the lesion as benign or malignant. It has been shown that cancer cells exhibit altered local electrical impedance. However, existing technology to measure the impedance of the breast has poor spatial resolution. We proposed to map the tissue impedance distribution with high spatial resolution, in conjunction with MRI to improve diagnostic accuracy of screening.

During the second year of this project, we improved the quality of conductivity images and conducted in vivo experiments. Several issues such as non-linearity in conductivity image reconstruction, out of slice effects were investigated. Improved reconstruction methods were studied. Multi-slice capability is added to the pulse sequence and various approaches were tested. Although it was not originally in the project proposal, we started collecting Contrast Enhanced MRI images to localize the tumor better.

A serious malfunction in the MRI receiver unit caused a delay of more than six months. A no-cost extension was requested to collect more conductivity images from animals and complete this project successfully.

Another conference manuscript was prepared and presented and a journal article was submitted.

14. SUBJECT TERMS Diagnosis of metastatic cancer, magnetic resonance imaging, electrical impedance imaging, electrical impedance scanning, MRI current density imaging, finite element	15. NUMBER OF PAGES 43
	16. PRICE CODE

17. SECURITY CLASSIFICATION OF REPORT Unclassified	18. SECURITY CLASSIFICATION OF THIS PAGE Unclassified	19. SECURITY CLASSIFICATION OF ABSTRACT Unclassified	20. LIMITATION OF ABSTRACT Unlimited

NSN 7540-01-280-5500

Standard Form 298 (Rev. 2-89)
Prescribed by ANSI Std. Z39-18
298-102

Table of Contents

INTRODUCTION:

In screening of breast cancer, once abnormalities or lesions are discovered by the X-ray mammogram, generally, other imaging techniques are needed as an adjunct to diagnose the lesion as benign or malignant. It has been shown that cancer cells exhibit altered local electrical impedance [4]. However, existing technology to measure the electrical impedance of the breast relies on a device that has poor spatial resolution [2,3]. We proposed to map the impedance distribution in the tissue with high spatial resolution, by using it in conjunction with Magnetic Resonance Imaging (MRI) to improve diagnostic accuracy of screening. For this purpose, we proposed: (1) To develop and optimize the necessary hardware and software for MRI based impedance imaging and interface it with the 4T MRI system, (2) Test the method on phantoms and an animal model of breast cancer and (3) Optimize the imaging parameters for minimizing false negatives and positives.

BODY

Overview of the Pulse Sequence:

In the first year, we had determined that a spin-echo based sequence with multiple 180^0 RF refocusing pulses provided best performance in terms of high sensitivity, high resolution and duration of data acquisition.

In Magnetic Resonance Electrical Tomography (MREIT) experiments that utilized this pulse sequence, sinusoidal current is injected into an object and the resulting magnetic fields are measured using a modified spin-echo sequence (Fig.1) [1]. The component of current-generated magnetic field parallel to the main static field (z-component) produces a phase shift. By synchronizing successive π pulses to half cycles of the current, this phase shift accumulates and is given in the final image as $\varphi(\mathbf{r}) = 4 \cdot \gamma \cdot N \cdot b(\mathbf{r}) / \omega$, where γ is the gyromagnetic ratio, N the number of cycles of injected current, $b(\mathbf{r})$ the amplitude of z-component current-generated magnetic field at point $\mathbf{r}$, and ω the angular frequency of the injected current. Hence, measurement of this phase shift allows for calculation of the (z-component) magnetic field distribution.
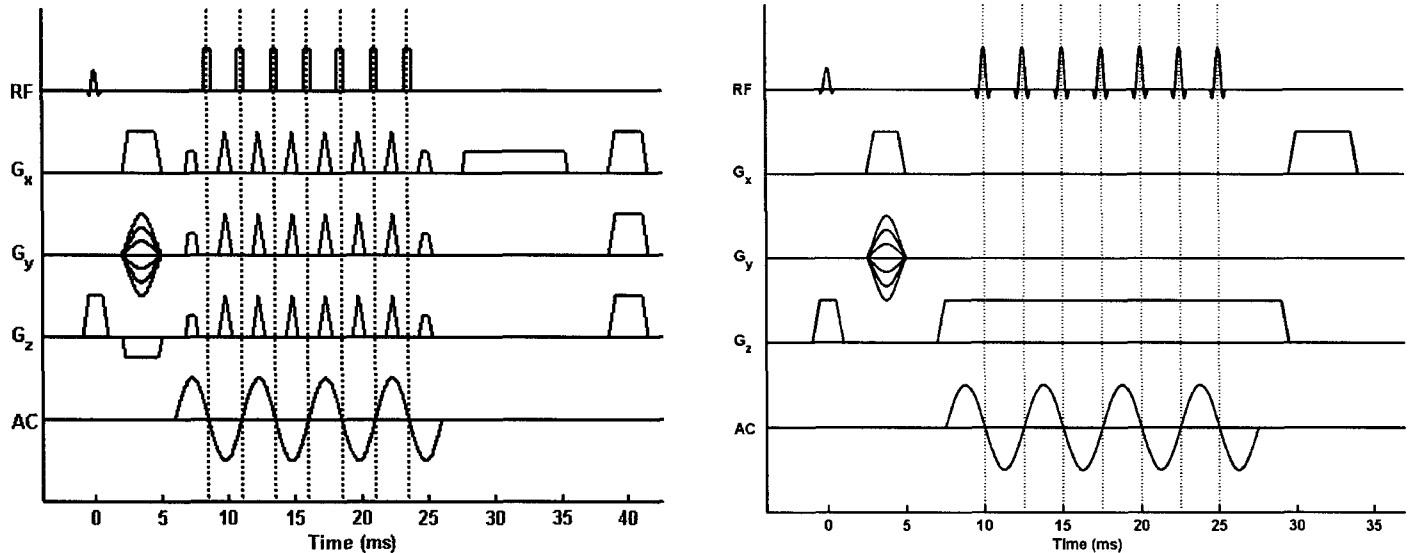

Figure 1 – The two versions of the MREIT pulse sequence for multi-slice conductivity imaging. The one on the left uses hard refocusing RF pulses and the one on the right uses 1.3ms long selective refocusing pulses.

Pulse Sequence Improvements: That pulse sequence was originally developed for single slice imaging. That was preferred because very short duration non-selective (wide band) radio frequency (RF) 180 refocusing pulses could be used. Short duration is required because those pulses are applied at zero crossings

of the injected current and long duration would interfere with non-zero values of injected current and cause abnormal slice profile, dephasing within slice, etc. For multi-slice imaging, those hard pulses cause significant spurious echos because they flip spins within the whole volume. In the second year, slice selective 3 lobe sinc pulse and non-selective hard pulse with strong crusher gradients and Car-Purcell-Meiboom-Gill (CPMG) echos were tested for multi-slice MREIT. It was found that hard pulses with alternating phase ($\pm 180^0$) and strong crushers resulted in acceptable slice profile and minimum artifacts. Duration of hard pulses was 250μs.

Although it was not included in the original grant application, we expect that multi-slice acquisition with 3D Finite Element Modeling and reconstruction will improve conductivity images further. Therefore, our future plans also include 3D reconstruction, and development of multi-slice imaging was crucial for our future improvements.

Overview of Impedance Image Reconstruction:

In the original application, a linear relationship between conductivity and corresponding magnetic field perturbations was proposed to reconstruct impedance images from the measured magnetic field maps. This is only a first order approximation and strong non-linearity between actual and reconstructed conductivity maps was observed in the studies we conducted in the second year. The details will be given in the next sections.

In the linear approximation, $\Delta B(r) = S(r,r') \Delta\sigma(r')$ is assumed, where $\Delta B(r)$ is the change in magnetic field at point r for a given current injection scheme resulting from a change $\Delta\sigma(r')$ in the conductivity at point r'. To compute S, the Finite Element Method (FEM) is utilized, whereby the object domain is discretized and S becomes a 'sensitivity' matrix. The matrix component S_{ij} is the change in magnetic field ∂B_i of element i with respect to a change in the conductivity $\partial\sigma_j$ of element j. An initial conductivity distribution σ_0 is assumed (e.g. uniform conductivity), the conductivity of a given element j perturbed by $\Delta\sigma_j$, the resulting ΔB calculated by the FEM, and matrix components approximated as $S_{ij} = \Delta B_i / \Delta\sigma_j$. The linear approximation can be inverted to yield $\Delta\sigma = \sigma_{final} - \sigma_{initial} = S^{-1} \Delta B = S^{-1} (B_{final} - B_{initial})$, where $\sigma_{initial}$ is the assumed initial (uniform) conductivity distribution, $B_{initial}$ the magnetic field distribution given $\sigma_{initial}$ and solved using the FEM, σ_{final} the actual conductivity distribution, B_{final} the MRI measured magnetic field distribution, and S^{-1} a truncated pseudoinverse calculated using singular value decomposition. Hence, the conductivity distribution of an object can be computed as $\sigma_{final} = S^{-1} (B_{final} - B_{initial}) + \sigma_{initial}$.

New Phantom Studies:

A series of phantom studies were conducted to further test the spatial resolution and dynamic range of contrast for MREIT. They were similar to what has been reported before but this time, the modified pulse sequence was used, and several issues such as variations and linearity of relative conductivity images were investigated. Several agarose gel phantoms with different conductivity distributions were prepared for these tests. The gels were placed inside an acrylic cylinder with an inner diameter of 7cm and height of 1cm. The conductive gels consisted of 2% (g/100mL) agarose and varying concentrations of Sodium Chloride (NaCl). During imaging, the axis of the cylinder was placed parallel to the z-axis (direction of the MRI magnetic field). Four electrodes made of copper foil, each 3mm wide, were placed at 0^0, 90^0, 180^0 and 270^0 along the inner wall and used to inject currents into the interior region. For each phantom, data were collected twice for two current injection schemes and used simultaneously in conductivity reconstruction. The first time, current was injected between the electrodes at 0^0 and 180^0, and the second time between the ones at 90^0, and 270^0. In the preliminary studies conducted, it has been empirically verified that this scheme improves the sensitivity and spatial resolution compared to using a single pair of electrodes.

For each phantom configuration, two separate data sets were collected by injecting 6 cycles of 2mA or 4mA 200Hz current into the phantom. All data were collected using the previously outlined pulse sequence with the following parameters: repetition rate (TR)=500ms, echo time (TE)=40ms, slice thickness=1cm, Field-of-View (FOV)=10cm, data matrix 64x64 and number of excitations (NEX)=8 (i.e. # signal averages). The z-component of current-generated magnetic field distributions were calculated from the resulting data and the conductivity distributions computed using the method outlined above.

Results

Conductivity images were first reconstructed using the linear approximation method outlined in the previous section. In the calculation of the inverse of **S** using Singular Value Decomposition (SVD), highest 200 singular values were used and the rest were truncated to minimize noise while preserving essential information. This value was also determined experimentally to be an optimum level for truncation. In the FEM mesh, 512 triangular elements were used.

Impedance Contrast Phantoms:

For contrast studies, a 16mm diameter inner disk of gel surrounded by a background of 1% NaCl was used. Two experiments were carried out with two similar contrast phantoms, where the inner disk contained either 4% or 10% NaCl. In the preliminary tests, it has also been experimentally verified that conductance scales sufficiently linearly with NaCl concentration. Therefore, the conductivity contrast values were approximately 1/4 and 1/10, respectively. Fig. 2 illustrates the standard spin-echo MRI image acquired from the contrast phantom (with 1/4 conductivity contrast). As seen in the figure, it is difficult to distinguish the two compartments in the MRI image. Fig. 3 shows conductivity images obtained from the 1/10 and 1/4contrast phantoms with 2mA injected current. Higher conductivity regions are greatly enhanced in the resulting images. The means and standard deviations of the reconstructed relative conductivity values in the two compartments inside the contrast phantoms were calculated and given in table I.
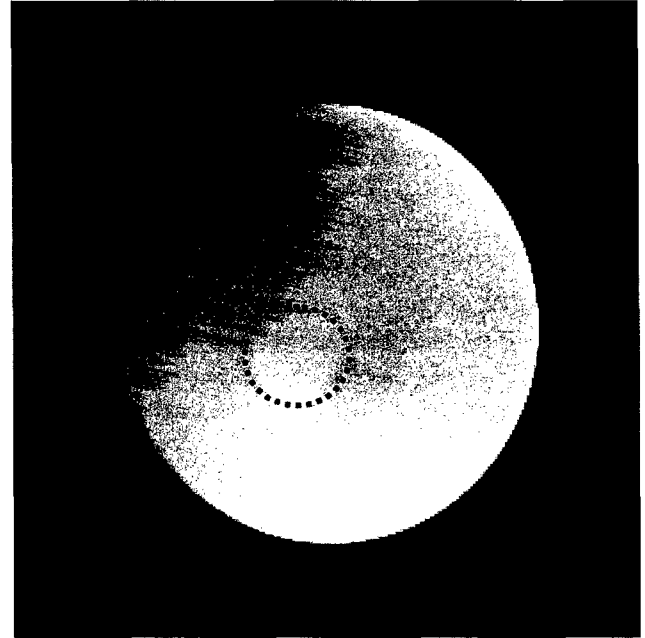

Fig.2. Spin-Echo image of 1/4 contrast phantom. The higher conductivity region is marked with red dashed lines and it is barely distinguishable in the MR image.

	$\sigma_o/\sigma_i = 1/4$ phantom (mean / std)		$\sigma_o/\sigma_i = 1/10$ phantom (mean / std)	
	I=2mA	I=4mA	I=2mA	I=4mA
Inside small disk (σ_{ir})	235.4 / 10.5	229.6 / 18.4	233.4 / 15.4	226.6 / 21.2
Background (σ_{or})	81.2 / 18.3	63.8 / 14.7	50.1 / 17.9	36.1 / 12.3

Table.1. Mean and standard deviation of relative conductivity (σ) values in contrast phantoms calculated by the MREIT method. Results are reported for both of the injected current amplitudes.

Fig. 4 shows the relationship between relative object conductivity values and relative MREIT image conductivity values as measured from the images given in figure 3.b. Since the background conductivity is kept the same for all contrast experiments, the background conductivity values (σ_{or}) were all normalized to 100 and the corresponding relative conductivity values for the small disks were normalized with the corresponding scaling factor for each image. Thus, the relative changes in object conductivity and corresponding conductivity value in the MREIT images were plotted. The plots are given for both 2mA and 4mA injected current cases. A non-linear relationship is observed in these plots. Moreover, the curves are slightly different for two different injected currents.
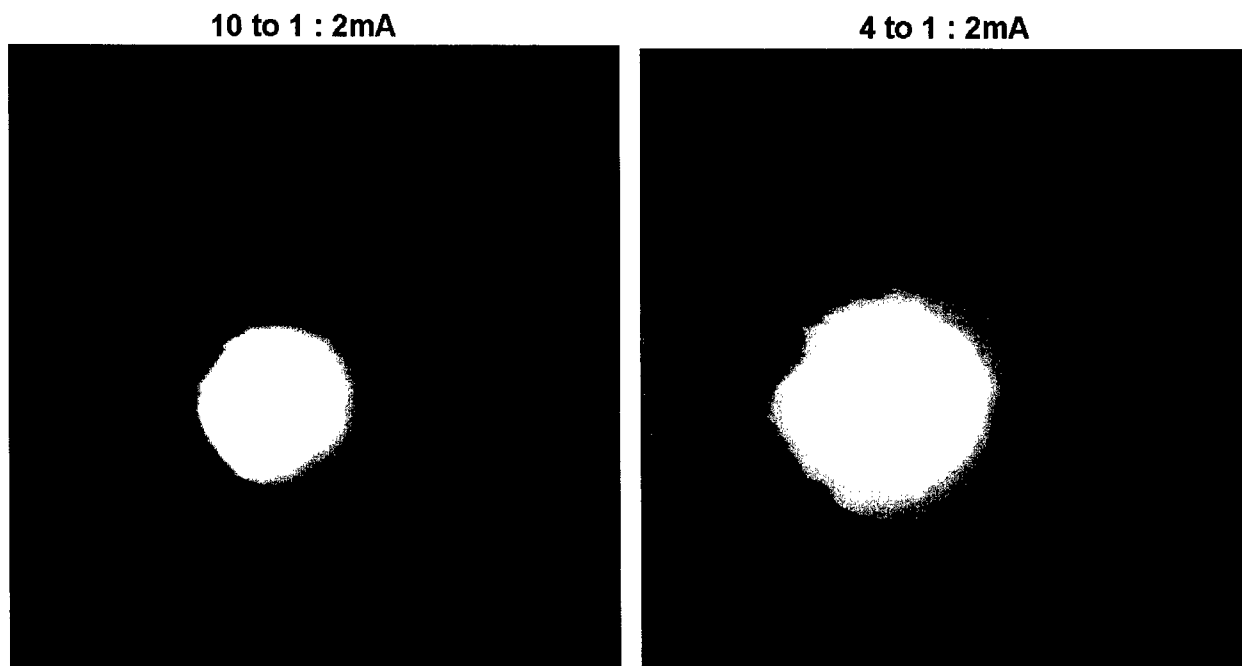
Fig.3. Conductivity images of 1/10 contrast (left) and 1/4 contrast (right) with 2mA current injection case. Those images were reconstructed with linearity approximation.
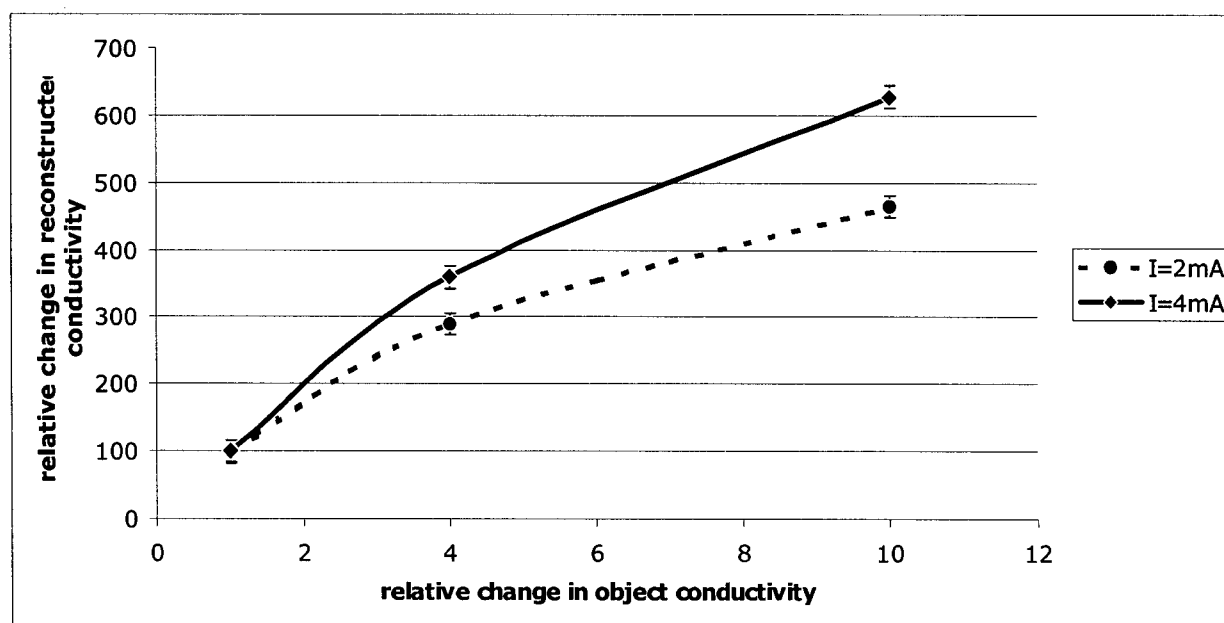

Fig.4. The plots of relative conductivity changes in the object versus relative conductivity values obtained from MREIT images. Plots are given for both of the injected current amplitudes. Error bars are also included in these plots.

Spatial Resolution phantom:

For the resolution phantom, two hollow nylon disks, each 16mm in diameter, were placed inside the larger disk. They were separated by 17mm center to center. The nylon shells acted as insulators, and each small disk was filled with the same gel as the surrounding background. Fig.5 shows the conductivity image of the

"spatial resolution phantom" with two identical nylon disks. The results of two experiments with 2mA and 4mA current injections are given in this figure. The gradually decreasing distance between the two small disks was used to assess the spatial resolution capability of conductivity images. A cross sectional profile is shown in Fig.6. Even though the contrast was somewhat reduced due to low-pass filtering of the point spread function, the 1mm separation could still be observed.

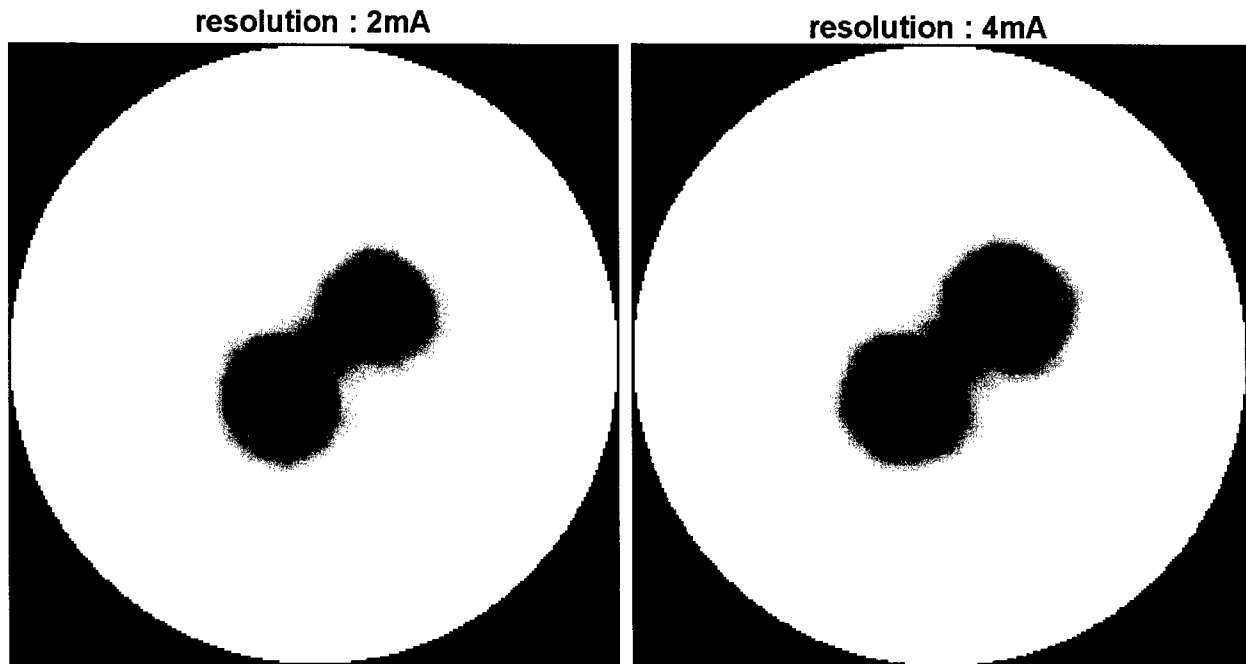**resolution : 2mA** **resolution : 4mA**

Fig.5. Conductivity images of resolution phantom with 2mA and 4mA current injection cases. Small dark circular areas show high conductivity compartments (insulating disks)
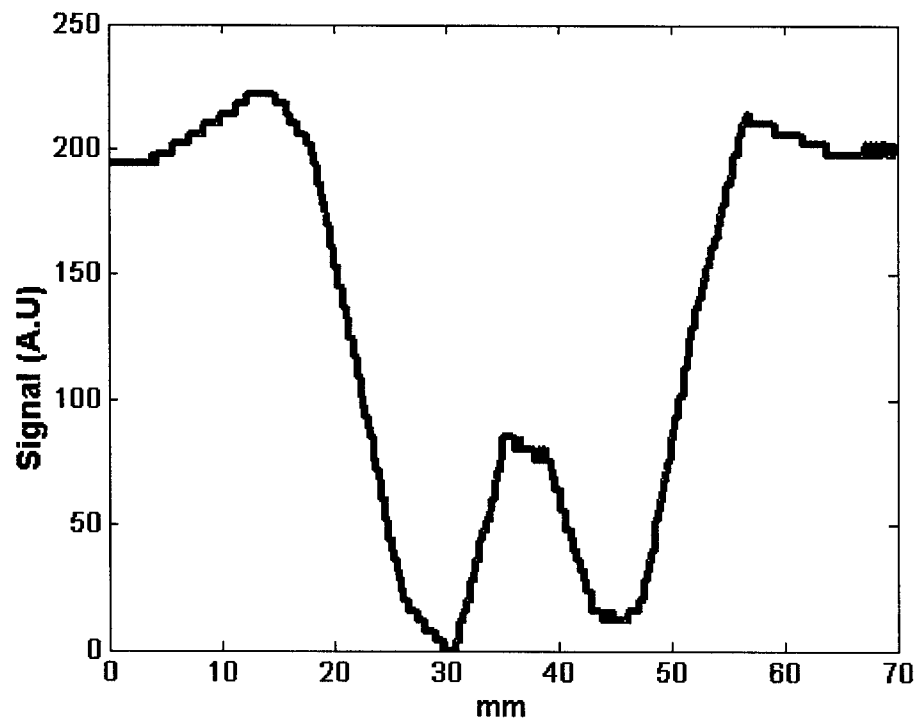

Fig.6. A profile taken diagonally from the conductivity image of resolution phantom going through the centers of the small disks. This profile is given for the 4mA current injection case

Animal Experiments:

Several MREIT experiments were also performed for in vivo impedance imaging of rats bearing tumors. For this purpose, a special animal holder was prepared from acrylic sheets. This holder helped keep the animal stationary during imaging. It also allowed for the placement of the electrodes in consistent positions for longitudinal studies. Electrodes were placed on acrylic hollow tubes filled with CuSO4 solution to detect the electrode positions precisely in the images. Initial experience has shown that the precise localization of electrode positions is essential for accurate reconstruction of impedance images. Current carrying wires ran along these tubes, which were in z-direction. This is essential to minimize interference from the magnetic fields generated by current in the wires. Prior to imaging, the animal was anesthetized by IV injection of ketamine and xylazine and then placed inside the holder. The electrodes were covered with a thin layer of conductive gel to provide good electrical contact. The skin areas of contact were shaved for better conductance.

An anatomical image was collected using FSE sequence prior to the MREIT images. The data matrix was 256X256, FOV = 10cm, slice thickness = 6mm TR = 4s, TE = 20ms/100ms NEX = 4. MREIT images were collected using the previously outlined pulse sequence with TR=500ms, TE=30ms, NEX=8 (signal averages), 64X64 data matrix, FOV = 10cm, slice thickness = 6mm, with an AC current of 1mA peak, 200Hz, 4 cycles.

Contrast enhanced MR images (CE-MRI) were also collected using Gd-DTPA, which is a well-established method to detect malignant tissues. Since vascular growth is greatly enhanced in tumor structures, contrast agent uptake of tumor sites increases with respect to normal tissues. In addition to that, interstitial compartment in tumors are large compared to normal structures, so the wash-out of contrast agent is also slower in tumors. Therefore, if two images are collected, one pre-contrast and the other post-contrast, the difference image yields enhanced pixel intensity in the areas of tumor growth. In this study, the goal was to verify the potential of MR-EIT to detect tumors. Contrast enhanced images were collected using a gradient-echo sequence with a 64X64 data matrix, FOV = 10cm, 6mm slice thickness, TR = 150ms, TE = 5ms, and 45^0 flip angle. One pre-contrast image was acquired before Gd-DTPA injection and a post-contrast image was collected 3 minutes after injection (Gd-DTPA: a commonly used MRI contrast agent).

The first step in animal imaging is the construction of the finite element mesh using an anatomical high resolution MRI image. The FEM mesh shown in Fig.7 consists of 702 nodes and 1268 first order triangular elements. Exact electrode locations are found using the markers in the animal setup and used for the boundary condition determination. The relative conductivity distribution was computed as described above and overlaid on the anatomical image (Figure 8.a). The resulting images show the higher conductivity regions with high contrast. Similarly, the contrast enhancement by Gd-DTPA is illustrated in figure 8.b. To investigate how the two images spatially
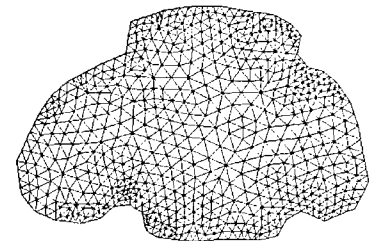

Fig.7. FEM mesh constructed from the anatomical MR Image

Fig.8. Axial slices from an SD rat inoculated with a R3230 AC tumor showing: (a) Conductivity; (b) CE-MRI; and (c) spatial correlation of CE-MRI and MREIT. The tumor had spread to multiple foci surrounding the body. In (a), red shows high conductivity and blue shows low conductivity regions; whereas red regions in (b) shows enhancement by Gd-DTPA; Areas that have both high conductivity and also enhanced by contrast agent are shown in hot colors in (c).

Page 9

correlate, another image was generated by masking the CE-MRI image with the MREIT image regions that have conductivity values in the upper one-thirds of the full range. Figure 8.c. shows regions that have high conductivity and also enhanced by Gd-DTPA

Although the in vivo conductivity images acquired so far are not of diagnostic quality, it demonstrates our capability to carry out such studies. Fig.8 also shows the potential of MREIT in localizing tumors. We are currently working on the improvements of image reconstruction for MREIT images that has better diagnostic potential.

Image Reconstruction improvements:

As seen in Fig.4, the linearity approximation causes unwanted suppression of image contrast. Moreover, that method requires user involvement to choose truncation level for taking inverse of the sensitivity matrix. The inverse of S is calculated using singular value decomposition (SVD) and user has to manually select the eigenvalues and eigenvectors that should be truncated to minimize errors in inverse operation and reconstruction. Therefore, we improved our reconstruction technique using an iterative approach with Tikhonov regularization.

Several other techniques were proposed that uses the magnetic flux density measurements to reconstruct MREIT images [5] but those require derivative operator and is more sensitive to noise compared to the Sensitivity Matrix based approaches.

As briefly described in the previous sections, sensitivity matrix approximation starts from an initial conductivity distribution σ_{ini} and corresponding magnetic flux density b_{ini}. A linear set of equations giving the relation between conductivity perturbations and magnetic flux density measurements around initial values is obtained:

$$\Delta \mathbf{b} = S \Delta \sigma \tag{11}$$

where $\Delta \mathbf{b} = \mathbf{b} - \mathbf{b}_{ini}$ is the change in magnetic flux density with respect to initial, S is the sensitivity matrix, and $\Delta \sigma = \sigma - \sigma_{ini}$. S is calculated for known geometry, boundary conditions, and initial conductivity and given the measurements, $\Delta \mathbf{b}$, conductivity is calculated. The solution is found by solving the least squares problem:

$$\min \| S \Delta \sigma - \Delta \mathbf{b} \| \tag{12}$$

where $\| . \|$ is the L_2 norm. For most cases, above problem is ill-conditioned and a regularization method that computes an approximate solution through a regularization parameter is required. Tikhonov regularization is a widely used technique where the modified problem

$$\min \{ \| S \Delta \sigma - \Delta \mathbf{b} \|^2 + \lambda \| \Delta \sigma \|^2 \} \tag{13}$$

is solved where λ is the regularization parameter. Two goals of regularization are minimizing the residual norm while keeping the solution norm being too large. There are two kinds of methods for the selection of the regularization parameter. If some knowledge on noise level in the data is available, the discrepancy principle can be used to find the regularization parameter. If no prior noise information is used, "L-curve" is widely used as a convenient graphical tool to set λ. The L-curve is a logarithmic plot of the solution norm versus the residual norm for each value of regularization parameter. The point, which has the shortest distance to origin is automatically selected as optimum λ and used in equation (13). Once the conductivity is found, it is assumed as the initial conductivity for the next iteration and the problem is solved in a nonlinear manner.

This technique was applied to the phantom data and the results are presented in Fig.9. It is clearly seen that the artifacts on the boundary of the object is corrected after 6 iterations. Another advantage of this reconstruction is that it does not require user input to select eigenvectors to be discarded. Everything runs automatically.

iteration 1   iteration 2
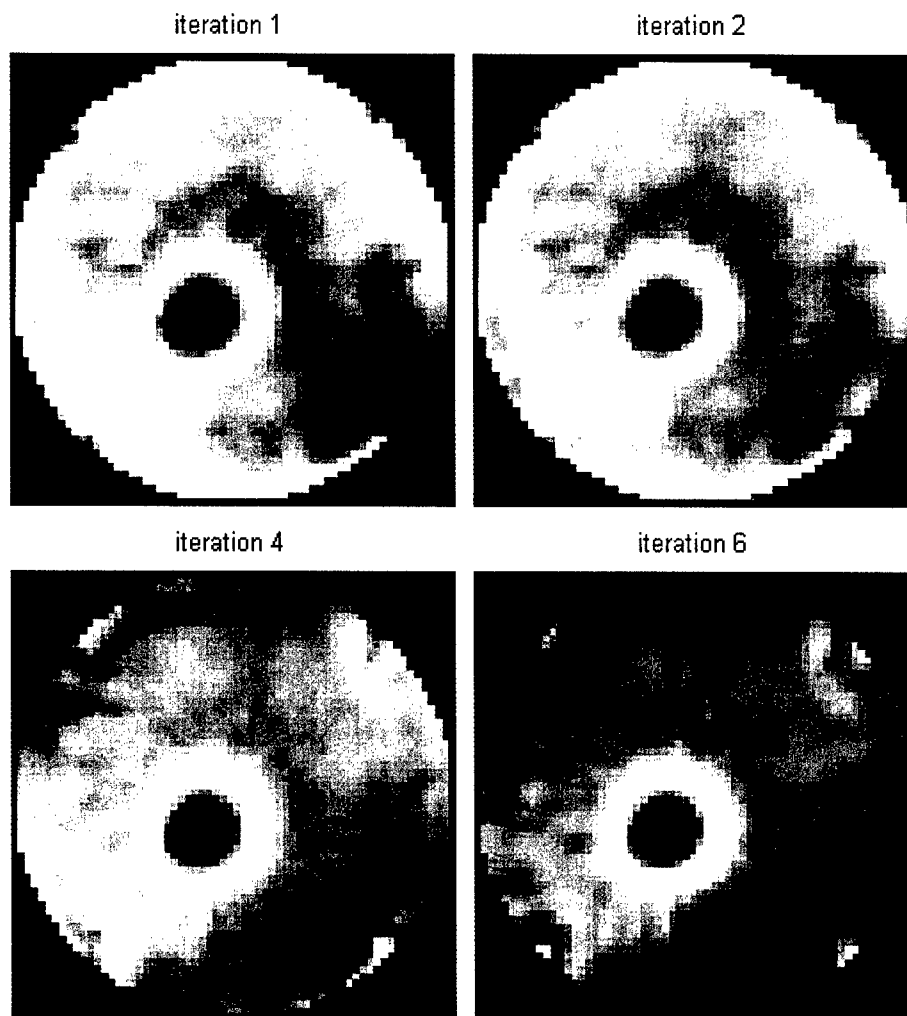
iteration 4   iteration 6

Fig.9. Iterative reconstruction of 1/10 conductivity contrast phantom with Tikhonov regularization. Results are shown for iterations 1, 2, 4 and 6. Note that the artifacts that show falsely as high conductivity on the boundary of the object disappear after 6th iteration.

Equipment Failures:

In May-June 2003, we experienced problems in the MRI console RF unit. Several experimental data had to be discarded because of equipment failure at random intervals during data acquisition. We first attempted to repair it ourselves but could not succeed. A repair by the manufacturer was also costly and was not worth for such an old version. Therefore, a new and improved RF unit was ordered and purchased. But all imaging operations had to stop with the Magnetic Resonance Research Systems (MRRS; formerly known as SMIS: Surrey Medical Imaging Systems) console during the period between June and November 2003. The unit was ordered in early August and was shipped at the end of October. By late November, we resumed our experiments but those failures delayed us by at least 6 months. Therefore, we requested a one-year no-cost extension to complete this project successfully. Several E-Mail communications were attached in the appendix about this RF unit issue.

KEY RESEARCH ACCOMPLISHMENTS

- The p ulse s equence w as m odified f or m ulti-slice a cquisition a nd v arious o ptions w ere t ested f or b est performance.

- Efficacy and problems of conductivity image reconstruction algorithm were determined with phantom tests.

- Fully automated and better conductivity image reconstruction method that minimized artifacts were investigated, developed and tested.
- Method was tested on several animals and conductivity images were obtained. Although it was not included in the original application, Contrast Enhanced MRI was added to the protocol as a gold standard to obtain better tumor localization.

REPORTABLE OUTCOMES:

- We have submitted one conference paper to the 2004 conference of International Society of Magnetic Resonance in Medicine (ISMRM). It is peer-reviewed and accepted for presentation and publication in conference proceedings (Proceedings of the 11th meeting of Intl. Soc. Mag. Res. Med., Page 1986, 2004, Kyoto, Japan).
- One manuscript is also prepared and submitted to "Technology in Cancer Research and Treatment" Journal (Adenine Press, http://www.tcrt.org). Copies of those papers are also included in the appendix.

CONCLUSIONS:

During the second phase of this project, we modified the pulse sequence for multi-slice acquisition for future improvements such as 3D reconstruction. 2D Reconstruction has limitations and it is prone to errors due to contamination from out-of-slice currents. Further investigations were carried out on phantoms to assess limitations and performance (SNR, linearity, etc) of the original reconstruction method. More robust reconstruction with regularization was developed to minimize artifacts.

The method was also applied to a small number of animals (N=5) induced with malignant tumors (R3230 AC) and conductivity images were reconstructed. Although conductivity images are not of diagnostic quality, yet, we are working on the new reconstruction technique to improve the quality. CE-MRI was added to the protocol for tumor localization and significant overlap with conductivity images were seen.

RF unit failure delayed our studies and a one-year no-cost extension was requested and granted. More in vivo data will be collected as proposed in our application and results will be reported during this extension.

The outcomes obtained so far are in accord with our hypothesis and we have successfully completed most of the steps outlined in the original project proposal.

REFERENCES:

[1] Mikac U. et al, MRI 19: 845 856 (2001)

[2] Malich, T. Fritsch, R. Anderson, T. Boehm, M. G. Freesmeyer, M. Fleck, and W. A. Kaiser, "Electrical impedance scanning for classifying suspicious breast lesions: first results," *European Radiology*, vol. 10, pp. 1555-61, 2000.

[3] Malich, T. Boehm, M. Facius, M. G. Freesmeyer, M. Fleck, R. Anderson, and W. A. Kaiser, "Differentiation of mammographically suspicious lesions: evaluation of breast ultrasound, MRI mammography and electrical impedance scanning as adjunctive technologies in breast cancer detection," *Clinical Radiology*, vol. 56, pp. 278-83, 2001.

[4] J. Surowiec, S. S. Stuchly, J. B. Barr, and A. Swarup, "Dielectric properties of breast carcinoma and the surrounding tissues," *IEEE Transactions on Biomedical Engineering*, vol. 35, pp. 257-63, 1988.

[5] H. S. Khang, B. I. Lee, S. H. Oh, E. J. Woo, S. Y. Lee, M. H. Cho, O. Kwon, J. R. Yoon, and J. K. Seo, "J-Substitution Algorithm in Magnetic Resonance Electrical Impedance Tomography (MREIT): Phantom Experiment for Static Resistivity Images," *IEEE Trans. on Medical Imaging*, vol. 21, no. 6, pp. 695-702, 2002.

APPENDIX

1) Three E-Mail printouts regarding the RF unit failures and purchasing of the new unit.

2) Quote for the new RF unit.

3) ISMRM 2004 conference paper.

4) MREIT paper submitted to TCRT journal

To: "David Taylor" <david.taylor@mrresearchsystems.com>
From: Tugan Muftuler <muftuler@uci.edu>
Subject: RF unit repair
Cc: geoff.fisher@mrresearchsystems.com
Bcc:
X-Attachments:

Dear David and Geoffrey,

We are having problems with our RF/interface unit. We have the old analog RF unit and interface board.
First, the received signal is not stable. Sometimes we observe oscillations on top of FID, sometimes
we do not see any FID at all. Oscillations cause either a "zipper artifact" like the ones you see if
there is RF penetration and sometimes two bright spots appear, which are symmetrically placed about
the origin (if one is at (x,y) the other one is at (-x,-y)). It is not RF penetration into the MRI
because we terminate the RF input with 50 ohm at the RF unit and it is still there.

Looks like we won't be able to buy a new RF unit in the near future, so I am looking into having the
second RF unit and interface board repaired. As you might recall we had two sets of SMIS systems. The
second unit does not give us any signal at all. So it is completely dead. Besides, it does not have DC
correction and other updates on it.

So, if I send that RF unit and interface board to you, can you repair them and add the DC correction
modifications and upgrades? If you can, what would be the approximate cost and time it would take to
do the repairs?

Once again, your immediate response will be greatly appreciated.

Best regards,

Tugan

```
X-From_: steve.roberts@mrresearchsystems.com  Tue Aug 12 02:21:32 2003
From: "Steve Roberts" <steve.roberts@mrresearchsystems.com>
To: <muftuler@uci.edu>
Subject: Receiver upgrade
Date: Tue, 12 Aug 2003 10:05:48 +0100
X-Priority: 3
X-UCIRVINE-MailScanner: No viruses found
```

Tugan,

I have attached the revised quote for the receiver upgrade with a brief section on warranty repair and returns.

Regards

Steve

 335b Tugan.doc

X-From_: steve.roberts@mrresearchsystems.com Fri Oct 31 09:27:21 2003
From: "Steve Roberts" <steve.roberts@mrresearchsystems.com>
To: "Tugan Muftuler" <muftuler@uci.edu>
Subject: Re: Receiver modules
Date: Fri, 31 Oct 2003 17:27:13 -0000
X-Priority: 3
X-UCIRVINE-MailScanner: No viruses found, No viruses found

Hi Tugan,

Yes, all the parts specified in the quotation have been shipped. The DHL Air Waybill number for this shipment is: 379 3862 914. Have a good weekend.

Regards

Steve

          ----- Original Message -----
          From: Tugan Muftuler
          To: Steve Roberts
          Sent: Friday, October 31, 2003 5:23 PM
          Subject: Re: Receiver modules

          Hi Steve,

          I just wanted to make sure: you said digital receiver modules are shipped but I am assuming that package includes the new modular interface unit, too.

          Thanks,

          Tugan

QUOTATION NO: 335b

MR Research Systems Ltd

Date: 12th August 2003

Unit 1K
Merrow Business Centre
Guildford, UK
GU4 7WA

To: Tugan Muftuler / Nabil Saba
Centre for Functional Onco-Imaging
Irvine Hall 164
University of California
Irvine
CA 92697-5020
USA

Tel: 44 1483 532146
Fax: 44 1483 838954
sales@mrresearchsystems.com

Description	TOTAL
Digital receiver upgrade package including decimator module, fast ADC module, additional PSU, new interface module and cable set	US$ 24,280
Total (excluding installation)	US$ 24,280
With 10% discount	US$ 21,852
On-site installation estimated 3 days (including expenses)	US$ 4,500
Total (including discount and installation)	**US$ 26,352**

Prices include carriage and insurance but exclude import duties and local taxes.

Terms of Payment: 50% with order, 50% on delivery
Delivery: 8-10 Weeks
Warranty: 12 months from delivery
Return Policy: MR Research Systems are responsible for the repair of delivered goods during the first 12 months. All shipping charges for returned faulty goods during the warranty period are at the expense of MR Research Systems. MR Research Systems will quote separately for the repair of goods outside the warranty period.

VAT REGISTRATION NO. 689 2725 79

A Comparison of MRI Based Electrical Impedance Imaging and Contrast Enhanced MRI of Tumors

L. Muftuler[1], M. Hamamura[1], O. Birgul[1], O. Nalcioglu[1]

[1]Functional Onco-Imaging Center, University of California, Irvine, CA, United States

Purpose

Malich et al has reported that the electrical impedance of malignancies could be 20-40 times lower than healthy tissues and benign formations [*Malich A. et al, Eur. Radiol. 10: 1555-1561 (2000)*]. Therefore, in-vivo impedance imaging of suspicious lesions could aid in improving the sensitivity and specificity of detecting malignant tumors. MRI based impedance imaging is a novel method, in which weak electrical currents are injected into the tissue and the resulting perturbations in magnetic field were measured using MRI. On the other hand, contrast enhanced imaging is a well-established method to detect malignant tissues. Since vascular growth is greatly enhanced in tumor structures, contrast agent uptake of tumor sites are increased with respect to normal tissues. In addition to that, interstitial compartment in tumors are larger compared to normal structures, so wash-out of contrast agent is also slower in tumors. Therefore, if two images are collected, one pre-contrast and the other post-contrast, the difference image will yield enhanced pixel intensity in the areas of tumor growth. In this study, our goal is to verify the potential of MR-EIT to detect tumors.

Methods

Sinusoidal current is injected into an object and the resulting magnetic fields are measured using a modified spin-echo sequence (Fig. 1) [*Mikac U. et al, MRI 19: 845 856 (2001)*]. The z-component of magnetic field (parallel to the main static field) generated by injected currents introduces a phase shift. By synchronizing successive π pulses to half cycles of the current, this phase shift accumulates and is given in the final image as $\varphi(r) = 4 \cdot \gamma \cdot N \cdot b(r) / \omega$, where γ is the gyromagnetic ratio, N the number of cycles of injected current, $b(r)$ the amplitude of z-component current-generated magnetic field at point r, and ω the angular frequency of the injected current. Hence, measurement of this phase shift allows for calculation of the (z-component) magnetic field distribution. To reconstruct conductivity image, a linear approximation $\Delta B(r) = S(r, r') \Delta \sigma(r')$ is assumed, where $\Delta B(r)$ is the change in magnetic field at point r for a given current injection scheme resulting from a change $\Delta \sigma(r')$ in the conductivity at point r'. S is calculated using Finite Element Method (FEM). The matrix component S_{ij} is the change in magnetic field ∂B_i of element i with respect to a change in the

Fig. 1. Pulse sequence used in MR-EIT

conductivity $\partial \sigma_j$ of element j. An initial conductivity distribution σ_0 is assumed (e.g. uniform conductivity), the conductivity of a given element j is perturbed by $\Delta \sigma_j$ and the resulting ΔB is calculated. S is inverted to obtain $\Delta \sigma = \sigma_{final} - \sigma_{initial} = S^{-1} \Delta B = S^{-1} (B_{final} - B_{initial})$, where $\sigma_{initial}$ is the assumed initial (uniform) conductivity distribution, $B_{initial}$ the magnetic field distribution given $\sigma_{initial}$, σ_{final} the actual conductivity distribution, and B_{final} the MRI measured magnetic field distribution. Hence, the conductivity distribution of an object is $\sigma_{final} = S^{-1} (B_{final} - B_{initial}) + \sigma_{initial}$.
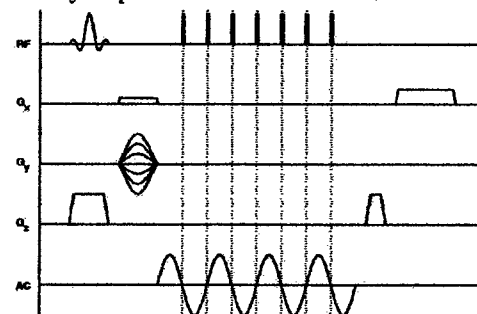
Results

An anatomical image was collected using FSE sequence prior to MR-EIT images. The data matrix was 256X256, FOV = 10cm, slice thickness = 6mm TR = 4s, TE = 20ms/100ms NEX = 4. MR-EIT images were collected using the previously outlined pulse sequence with TR=2s, TE=32ms, and NEX=8, 64X64 data matrix, FOV = 10cm, slice thickness = 6mm, with an AC current of 1mA peak, 200Hz, 4 cycles. Contrast enhanced images were collected using GE sequence with 64X64 data matrix, FOV = 10cm, 6mm slice thickness, TR = 150ms TE = 5ms and 45^0 flip angle. One pre-contrast image was acquired before Gd-DTPA injection and a post-contrast image was collected 3 minutes after injection. Relative conductivity distribution was computed as described above and overlaid on anatomical image (Fig. 2a). The resulting images clearly show the higher conductivity regions. Similarly, the contrast enhancement by Gd-DTPA is illustrated in Fig. 2b. Fig 2.c. shows regions that have high conductivity and also enhanced by Gd-DTPA. This image is generated by masking Gd-DTPA images with regions that have conductivity values in the upper one-third of the full range.
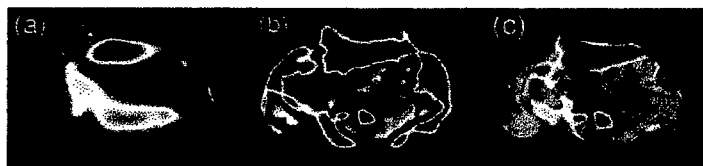

Fig.2. (a) Conductivity distribution. Red: high conductivity, blue: low conductivity; (b) difference of pre and post Gd-DTPA images. Red: regions enhanced by Gd-DTPA; (c) Areas that have both high conductivity and also enhanced by contrast agent.

Discussion

In this preliminary study, we have shown that MRI based impedance imaging can be used to detect malignant tumors. It can be seen from these results that there is high correlation between conductivity images and contrast enhanced images. Although they do not completely overlap, this is expected because the two methods emphasize different properties of tumors. For example, edema will most likely show high conductivity but will not show signal enhancement with Gd-DTPA. To exclude edema regions from conductivity images, one can use T2 weighted sequences that highlights edema. In this preliminary experiment, we imaged an animal with a large tumor size, which was currently available. In large tumors, various compartments like edema, necrosis and viable tumor cells exist and their conductivity and contrast agent enhancement will be different. Currently we are working on a longitudinal study to observe changes in conductivity as well as Gd-DTPA based contrast enhancement in tumor structures as the tumor grows. Gd enhanced images will be used to verify our results in vivo. At the end of the study, tumors will be excised and undergo histologic analysis. Contrast enhanced and T2 weighted images together with MR-EIT maps will allow us to assess how conductivity correlates with different compartments of tumors. Electrode position and number could be another factor that may confound detection of some low conductivity structures close to surface. We will also investigate effects of electrode placement in our future experiments.

Acknowledgements:

Resolution And Contrast In Magnetic Resonance Electrical Impedance Tomography (MREIT) and Its Application To Cancer Imaging

L. Tugan Muftuler* Ph.D., Mark Hamamura, M.Sc., Ozlem Birgul, Ph.D. Orhan Nalcioglu, Ph.D.

Tu & Yuen Center for Functional Onco-Imaging
University of California, Irvine

Correspondence should be addressed to: L. Tugan Muftuler
Tel: (949) 824 6290
e-mail: muftuler@uci.edu

Abbreviations:
MRI: Magnetic Resonance Imaging
EIT: Electrical Impedance Tomography
MREIT: Magnetic Resonance Electrical Impedance Tomography
FEM: Finite Element Method
EIS: Electrical Impedance Scanning
OPAMP: Operational Amplifier
SVD: Singular Value Decomposition
NEX: Number of Excitations
CE-MRI: Contrast Enhanced MRI

ABSTRACT

It has been reported that the electrical impedance of malignancies could be 20-40 times lower than healthy tissues and benign formations. Therefore, in-vivo impedance imaging of suspicious lesions may prove to be helpful in improving the sensitivity and specificity of detecting malignant tumors. Several systems have been developed to map the conductivity distribution inside a volume of tissue, however they suffer from poor spatial resolution because the measurements are taken only from surface electrodes. MRI based impedance imaging (MREIT) is a novel method, in which weak electrical currents are injected into the tissue and the resulting perturbations in the magnetic field are measured using MRI. This method has been shown to provide better resolution compared to previous techniques of impedance imaging because the measurements are taken from inside the object on a uniform grid. Thus, it has the potential to be a useful modality that may detect malignancies earlier. Several phantom imaging experiments were performed to investigate the spatial resolution and dynamic range of contrast of this technique. The method was also applied to a live rat bearing a R3230 AC tumor. Tumor location was identified by contrast enhanced imaging.

INTRODUCTION

Breast cancer is the leading cause of cancer deaths among women in many parts of the world and currently no single imaging modality has both high sensitivity and specificity for the diagnosis of breast cancer. At present, well-established breast screening methods have high sensitivity but suffer from poor specificity. X-ray mammography, which is accepted as the gold standard for breast cancer screening, provides high sensitivity but has a high rate of false-positives (2-4). Similarly, the sensitivity of breast MRI can be very high, however the specificity for the detection of abnormalities is variable (5, 6). In addition to the high rate of false positives, some of these techniques also fail to detect breast cancer in some cases, such as patients with dense breast tissue, which is common among younger patients, and patients undergoing hormone replacement therapy during post-menopausal period (7). New imaging modalities with better specificity may help reduce the rate of false positives, hence eliminate unnecessary biopsies.

It has been shown that electrical properties of malignant tissues are significantly different from those of normal and benign tissues. Surowiec *et al* have reported that the electrical impedance of malignant tumors decreases by a factor of 20 to 40 with respect to normal or

benign tissue (1). This information may be used in tumor detection and characterization. Therefore, the spatial distribution of conductivity measurements (which is inversely related to impedance) can be used in conjunction with other imaging modalities to identify tumors and achieve higher specificity rates compared to the currently used techniques.

Electrical Impedance Scanning (EIS) is a new technique recently introduced to aid in the diagnosis of malignant breast tumors (10-14). The device that uses this technique generates a map of the conductivity distribution inside the breast tissue. A probe that comprises of an array of electrodes is placed over the breast and small amounts of current are injected into the tissue through another electrode placed in the palm of the patient. Using the distribution of electric currents in this electrode array, the conductivity map is reconstructed. This device received FDA approval and has been introduced to the market (15). However, the conductivity images reconstructed using this technique have poor spatial resolution and are insensitive to tumors deep inside the breast, which are located 3-3.5cm away from the surface, and tumors just under the nipple. Moreover, the spatial resolution is not uniform throughout the imaging region.

Electrical Impedance Tomography (EIT) was developed in the 1980s to reconstruct the conductivity distribution inside a conducting volume. In this method, a current distribution is generated inside the object by injection or induction and peripheral voltage measurements are acquired to find the internal conductivity distribution (8). Although EIT is widely used for dynamic imaging, its potential application in breast cancer detection was also investigated (9). However, this method also suffers from poor spatial resolution due to the limited number of voltage measurements taken only from the surface. This imaging technique is also less sensitive to conductivity changes deep inside the object.

MREIT is a recently developed method for conductivity imaging (16-21). It uses the magnetic flux density measurements acquired from MR phase images to reconstruct conductivity. Magnetic flux density generated by applied currents can be measured with high spatial resolution using MRI. Various techniques have been proposed for DC (22), AC (23, 24), and RF (25) currents. Unlike EIT, the spatial resolution in the MREIT is position independent. However, it should be noted that only the component of the magnetic flux density in the direction of the main field of the MRI system can be measured. Therefore, one must develop a technique to solve the inverse problem of finding the conductivity or current density from only one component of magnetic flux density. With this technique, only the relative conductivity

values can be reconstructed from using only the magnetic flux density measurements. In order to find the absolute conductivity values, at least one voltage measurement from the boundary is required. The reconstruction algorithms can also be divided into two groups depending on the data type required. The first group uses magnetic flux density directly whereas in the second one, the current density distribution is required in image reconstruction. Algorithms that use current density distribution require the measurement of all three components of the magnetic flux density, thus rotation of the object inside the magnet is required. Obviously, this is not a practical situation.

In this study, the MREIT technique was tested on various conductivity phantoms to investigate its spatial resolution, signal-to-noise ratio (SNR) and contrast-to-noise ratio (CNR). Various phantoms were built with agarose gels mixed with NaCl to create compartments with known conductivity distributions. Preliminary data was also collected in vivo from Sprague-Dawley rats innoculated with the R3230 AC tumor. Contrast Enhanced MRI images were also collected to localize the tumor and investigate the spatial correlation between the outcomes of the two techniques.

MATERIALS AND METHODS

Data were collected by a 4T whole body MRI system that has a Magnex magnet (Magnex Scientific Inc., UK) equipped with a whole body gradient coil set (Tesla Eng. UK), which provides up to 3G/cm gradient fields. A 13 channel room-temperature high-order shim system with MXA-13-4 shim power supply (Resonance Research, Billerica, MA) is also available to minimize field inhomogeneities. This system is interfaced with a MRRS console (Magnetic Resonance Research Systems, Guildford, UK) that has broadband RF transmit and receive channels. A 16 leg, quadrature, high-pass birdcage coil with 10 cm diameter and 18 cm length was designed and built in-house for the MREIT experiments.

Pulse sequence

The pulse sequence used for the MREIT experiments is similar to a fast spin echo sequence, where a train of 180^0 RF pulses is applied following a 90^0 RF pulse (Fig.1). However, no phase encode or read-out gradients were applied between the 180^0 RF pulses and the data was collected with a single read-out gradient only after the last 180^0 RF pulse. Burst sine wave currents were injected into the object during the RF pulse train where each 180^0 RF pulse was applied at the

zero crossing of the sine waves. The duration of each 180^0 RF pulse was 1.3ms. A similar sequence was proposed by Mikac *et al* to obtain image of electric currents inside an object (24).

The z-component of magnetic field (parallel to the main static field) generated by the injected currents introduces a phase shift that accumulates over each half-cycle of the sine wave. The simplified MRI signal equation is given as:

$$s(u,v) = \iint M(x,y)\, e^{j\theta(x,y)}\, e^{j(xu+yv)}\, e^{j\gamma \int_0^t (b(x,y)\cos(\omega t))\, dt}\, dxdy \qquad [1]$$

$M(x,y)$ is proportional to the density of protons within a voxel at coordinates (x,y). The phase angle $\theta_{(x,y)}$ accounts for all the constant phase terms including static field inhomogeneity and other hardware related phase delays. The gyromagnetic ratio is shown by γ, and u and v in this equation are called the "spatial frequencies". They are defined as $u=\gamma * G_x * T_{Gx}$ and $v=\gamma * G_y * T_{Gy}$, where T_{Gx} and T_{Gx} represent the duration of the gradient pulses Gx and Gy, respectively. Therefore, in the final image the accumulated total phase at a pixel at location (x,y) due to the magnetic field generated by injected currents is:

$$\varphi(x,y) = 4 \cdot \gamma \cdot N \cdot b(x,y) / \omega \qquad [2]$$

where N is the number of cycles of injected current, $b(x,y)$ the amplitude of the z-component current-generated magnetic field at point (x,y), and ω the angular frequency of the injected current. Hence, measurement of this phase shift allows for calculation of the (z-component) magnetic field distribution.

During the experiments, the data was collected twice with opposite polarities of electric current, hence changing the polarity of current-generated magnetic field distribution. When resulting phase terms were subtracted, those coming from the static field inhomogeneities and delays in MRI hardware were eliminated, leaving only the terms caused by $b(x,y)$. To obtain the magnetic field distribution $b(x,y)$ from the acquired data, the MRI images were first reconstructed using the FFT. The resulting phase terms from the two sets of images were subtracted. Then, the magnetic field term was calculated using the expression given in equation [2].

Hardware: An HP ESG-4400B signal generator produced the sine waves. These signals were synchronized to the pulse sequence by a TTL pulse generated by the scanner computer. A transconductance amplifier was designed and built using three LM741 OPAMP circuits to convert the voltage from the signal generator into a current output. This experimental setup is

illustrated in figure 2. MRRS console controls the whole experiment, which generates the pulse sequence, acquires the incoming data, and synchronizes the external units. After data collection, raw MRI data (k-space) was exported to another Pentium PC for off-line processing.

Fig.2

Conductivity image reconstruction

As discussed in the previous sections, using MRI, one can only measure the magnetic field generated by the currents injected into an object. Moreover, only the field component that is parallel to the main field of the magnet can be measured. Therefore, one has to derive a relationship between the conductivity distribution inside an object and the measured magnetic field. If one needs to calculate the current density or precise conductivity distribution, all three orthogonal components of the magnetic field have to be measured. Then, Maxwell's equations can be utilized to find all three orthogonal components of the current density. However, this is only possible by rotating the object in three orthogonal directions inside the MRI system. This is not possible for human subjects. Rotation would also introduce problems with registration of measurements taken with different orientations of any object under investigation. Thus, a method that uses only the z-component of the magnetic field to calculate the conductivity distribution was adopted (16,20).

Sensitivity Matrix method: Since the relation between the conductivity distribution and the magnetic fields generated by the internal current distribution is nonlinear, one has to either employ iterative techniques or try to linearize around an initial value. In the presented study, the second approach was adopted, in which a linear relationship between the conductivity perturbations, $\Delta\sigma$, and magnetic field perturbations, ΔB, was assumed (16). This relationship is given in equation [3] as:

$$\Delta B_z = S \cdot \Delta\sigma \qquad [3]$$

If there are n conductivity elements and m measurement points, then $\Delta\sigma$ is an nx1 vector, ΔB is an mx1 vector and the "sensitivity matrix" S is an m x n matrix. The entry of the sensitivity matrix at i[th] row and j[th] column denotes the change in the ith field measurement due to a small change in conductivity of the jth element. Therefore, equation [3] can be written explicitly as:

$$
\begin{bmatrix} \Delta B_1 \\ \Delta B_2 \\ \vdots \\ \Delta B_m \end{bmatrix} = \begin{bmatrix} \dfrac{\partial B_1}{\partial \sigma_1} & \dfrac{\partial B_1}{\partial \sigma_2} & \cdots & \dfrac{\partial B_1}{\partial \sigma_n} \\ \dfrac{\partial B_2}{\partial \sigma_1} & \dfrac{\partial B_2}{\partial \sigma_2} & \cdots & \dfrac{\partial B_2}{\partial \sigma_n} \\ \vdots & \vdots & \ddots & \vdots \\ \dfrac{\partial B_m}{\partial \sigma_1} & \dfrac{\partial B_m}{\partial \sigma_2} & \cdots & \dfrac{\partial B_m}{\partial \sigma_n} \end{bmatrix} \begin{bmatrix} \Delta \sigma_1 \\ \Delta \sigma_2 \\ \vdots \\ \Delta \sigma_3 \end{bmatrix} \qquad [4]
$$

In order to calculate the "sensitivity matrix" **S** one must calculate the magnetic field map for a given conductivity distribution and current injection scheme. In order to calculate this, the electric potential distribution in the imaging slice is determined by solving Poisson's equation with Neumann boundary value conditions, which is stated as,

$$
\nabla \cdot (\sigma \nabla \phi)(x,y) = 0 \qquad (x,y) \in D
$$

$$
\sigma \frac{\partial \phi}{\partial n} = \begin{cases} J \text{ on positive current electrode} \\ -J \text{ on negative current electrode} \\ 0 \text{ elsewhere} \end{cases} \qquad [5]
$$

where σ is the electrical conductivity, ϕ is the electric potential and D is the slice of object to be imaged. The above problem is nonlinear in terms of conductivity since the electric potential itself is also conductivity dependent. The Finite Element Method (FEM) was used to calculate the distribution of the potential. Once ϕ is calculated, the electric field and current density distribution inside the imaging region may be found using the equations:

$$
\vec{E} = -\nabla \phi
$$

$$
\vec{J} = \sigma \vec{E} \qquad [6]
$$

Using equation [6], the magnetic field generated by this ohmic current can be calculated by the Biot-Savart law. The differential magnetic field can be written in terms of the differential current element $I d\vec{l}$ as,

$$
d\vec{B} = \frac{\mu_o I}{4\pi} \left(\frac{d\vec{l} \times \vec{R}}{R^3} \right) \qquad [7]
$$

where μ_o is the permeability constant and $\vec{R}$ is the vector from the source point at (x', y', z') to the field point (x, y, z). The relationship between the current and magnetic field is linear and the total magnetic field can be obtained by integrating equation [7] over all sources. Using equations 5-7, the magnetic field can be calculated for an assumed conductivity distribution.

The sensitivity matrix can be calculated using either a numerical or a semi-analytical approach. In the numerical approach, each column of the sensitivity matrix is calculated

separately by solving the forward problem by changing the conductivity of a single element. This approach requires the repetitive solution of the forward problem and increases the execution time. For faster reconstruction, the semi-analytical method was used for the calculation of the sensitivity matrix as explained in (20).

Once the sensitivity matrix S is calculated for a certain geometry, the generalized inverse, S^{-1}, is found by using singular value decomposition (SVD). Then, using the magnetic field measurements B_{meas} obtained from MRI, the conductivity distribution can be approximated by,

$$\Delta\sigma = S^{-1} \cdot \Delta B \qquad\qquad [8]$$

Where $\Delta B = B_{meas} - B_i$. This method has been tested both by simulation and experimental phantom studies and shown that a good approximation to the relative conductivity distribution map can be obtained (16,20).

Phantom Experiments

A series of phantom studies were conducted to test the spatial resolution and dynamic range of contrast for MREIT. Several agarose gel phantoms with different conductivity distributions were prepared for the tests. The gels were placed inside an acrylic cylinder with an inner diameter of 7cm and height of 1cm. The conductive gels consisted of 2% (g/100mL) agarose and varying concentrations of NaCl. During imaging, the axis of the cylinder was placed parallel to the z-axis (direction of the MRI magnetic field). Four electrodes made of copper foil, each 3mm wide, were placed at 0^0, 90^0, 180^0 and 270^0 along the inner wall and used to inject currents into the interior region. For each phantom, data were collected twice for two current injection schemes and used simultaneously in conductivity reconstruction. The first time, current was injected between the electrodes at 0^0 and 180^0, and the second time between the ones at 90^0, and 270^0. In the preliminary studies conducted, it has been empirically verified that this scheme improves the sensitivity and spatial resolution compared to using a single pair of electrodes.

For contrast studies, a 16mm diameter inner disk of gel surrounded by a background of 1% NaCl was used . Two experiments were carried out with two similar contrast phantoms, where the inner disk contained either 4% or 10% NaCl. In the preliminary tests, it has also been experimentally verified that conductance scales sufficiently linearly with NaCl concentration. Therefore, the conductivity contrast values were approximately 1/4 and 1/10, respectively.

For the resolution phantom, two hollow nylon disks, each 16mm in diameter, were placed inside the larger disk. They were separated by 17mm center to center. The nylon shells acted as insulators, and each small disk was filled with the same gel as the surrounding background.

For each phantom configuration, two separate data sets were collected by injecting 6 cycles of 2mA or 4mA (rms) 200Hz current into the phantom. All data were collected using the previously outlined pulse sequence with the following parameters: TR=500ms, TE=40ms, slice thickness=1cm, FOV=10cm, data matrix 64x64 and NEX=8. The z-component of current-generated magnetic field distributions were calculated from the resulting data and the conductivity distributions computed using the method outlined above.

Animal Experiments

An MREIT experiment was also performed for in vivo impedance imaging of a tumor bearing rat. For this purpose, a special animal holder was prepared from acrylic sheets. This holder helped keep the animal stationary during imaging. It also allowed for the placement of the electrodes in consistent positions for longitudinal studies. Electrodes were placed on acrylic hollow tubes filled with CuSO4 solution to detect the electrode positions precisely in the images. Initial experience has shown that the precise localization of electrode positions is essential for accurate reconstruction of impedance images. Current carrying wires ran along these tubes, which were in z-direction. This is essential to minimize interference from the magnetic fields generated by current in the wires. Prior to imaging, the animal was anesthetized by IV injection of ketamine and xylazine and then placed inside the holder. The electrodes were covered with a thin layer of conductive gel to provide good electrical contact. The skin areas of contact were shaved for better conductance.

An anatomical image was collected using FSE sequence prior to the MREIT images. The data matrix was 256X256, FOV = 10cm, slice thickness = 6mm TR = 4s, TE = 20ms/100ms NEX = 4. MR-EIT images were collected using the previously outlined pulse sequence with TR=500ms, TE=30ms, NEX=8 (signal averages), 64X64 data matrix, FOV = 10cm, slice thickness = 6mm, with an AC current of 1mA peak, 200Hz, 4 cycles.

Contrast enhanced MR images were also collected (CE-MRI) using Gd-DTPA, which is a well-established method to detect malignant tissues. Since vascular growth is greatly enhanced in tumor structures, contrast agent uptake of tumor sites increases with respect to normal tissues. In addition to that, interstitial compartment in tumors are large compared to normal structures, so

the wash-out of contrast agent is also slower in tumors. Therefore, if two images are collected, one pre-contrast and the other post-contrast, the difference image yields enhanced pixel intensity in the areas of tumor growth. In this study, the goal was to verify the potential of MR-EIT to detect tumors. Contrast enhanced images were collected using a GE sequence with a 64X64 data matrix, FOV = 10cm, 6mm slice thickness, TR = 150ms, TE = 5ms, and 45^0 flip angle. One pre-contrast image was acquired before Gd-DTPA injection and a post-contrast image was collected 3 minutes after injection.

RESULTS

Conductivity images were reconstructed using the method outlined in the methods section. In the calculation of the inverse of **S** using SVD, the highest 200 singular values were used and the rest were truncated to minimize noise while preserving essential information. This value was also determined experimentally to be an optimum level for truncation. In the FEM mesh, 512 triangular elements were used.

Impedance Contrast Phantoms: Figure 3.a illustrates the standard spin-echo MRI image acquired from the contrast phantom (with 1/4 conductivity contrast). As seen in the figure, it is difficult to distinguish the two compartments in the MRI image. The top row in figure 3.b shows conductivity images obtained from the 1/10 contrast phantom with two separate current amplitudes. Similarly, the bottom row of figure 3.b shows conductivity image of the 1/4 contrast phantom. Higher conductivity regions are greatly enhanced in the resulting images. The means of the reconstructed relative conductivity values in the two compartments inside the contrast phantoms were calculated and given in table I.

Table I
Fig.3

Figure 3.c shows the relationship between relative object conductivity values and relative MREIT image conductivity values as measured from the images given in figure 3.b. Since the background conductivity is kept the same for all contrast experiments, the background conductivity values (σ_{or}) were all normalized to 100 and the corresponding relative conductivity values for the small disks were normalized with the corresponding scaling factor for each image. Thus, the relative changes in object conductivity and corresponding conductivity value in the MREIT images were plotted. The plots are given for both 2mA and 4mA injected current cases. A non-linear relationship is observed in these plots. Moreover, the curves are slightly different for two different injected currents.

Fig.4

Spatial Resolution phantom: Figure 4.a shows the conductivity image of the "spatial resolution phantom" with two identical nylon disks. The results of two experiments with 2mA and 4mA current injections are given in this figure. The gradually decreasing distance between the two small disks was used to assess the spatial resolution capability of conductivity images. A cross sectional profile is shown in Figure 4.b. Even though the contrast was somewhat reduced due to low-pass filtering of the point spread function, the 1mm separation could still be observed.

In vivo Imaging: The first step in animal imaging is the construction of the finite element mesh using an anatomical high resolution MRI image. The FEM mesh shown in Figure 5.d consists of 702 nodes and 1268 first order triangular elements. Exact electrode locations are found using the markers in the animal setup and used for the boundary condition determination. The relative conductivity distribution was computed as described above and overlaid on the anatomical image (Figure 5.a). The resulting images show the higher conductivity regions with high contrast. Similarly, the contrast enhancement by Gd-DTPA is illustrated in figure 5.b. To investigate how the two images spatially correlate, another image was generated by masking the CE-MRI image with the MREIT image regions that have conductivity values in the upper one-thirds of the full range. Figure 5.c. shows regions that have high conductivity and also enhanced

Fig.5

by Gd-DTPA.

DISCUSSION

In this preliminary study, the potential of the MREIT method for obtaining in vivo conductivity information with good spatial resolution and sensitivity was demonstrated, which may be helpful in identifying malignant tumors.

In the results presented here, a fixed frequency of 200Hz was used for the applied electrical currents. This choice was based on previous studies that investigated electrical properties of tumors (7). Those studies have reported that a higher conductivity contrast was obtained with the application of 200Hz currents.

In contrast phantom tests, conductivity ratios of 1/4 and 1/10 were used. The method presented here clearly detected these conductivity perturbations in the objects. Based on the range of conductivity changes of malignancies compared to those of benign or healthy tissues that were reported in the literature (1), MREIT should offer sufficient sensitivity for the detection of malignancies. Although the minimum detectable conductivity perturbation by MREIT has not

been tested, from the results presented, it may be anticipated that much smaller changes could also be detected.

Since the reconstruction method used here is based on the linearity assumption between conductivity perturbations and measured magnetic fields, it only gives precise relative conductivity measurements for small conductivity perturbations within the object (or body). In the results presented here, the ratio of conductivity values measured in various compartments in the reconstructed images did not reflect the actual conductivity contrast. Since relatively large conductivity changes were used in the phantoms, it was observed that the conductivity contrast in the images was lower than the actual ratios due to the nonlinear nature of the actual relationship. The non-linear relationship between conductivity perturbations in the object versus perturbations in reconstructed EIT images was studied in detail by Ider *et al* (27). In addition to that, it can also be observed that the contrast in the conductivity images decreased slightly when the amplitude of the current was decreased from 4 to 2mA. Since the non-linear relationship between magnetic field distribution and conductivity values is assumed to be linear in the sensitivity matrix method, the degree of deviation from linearity will vary with changing current amplitude. As seen in the figure, the curve with 2mA current amplitude is slightly more linear compared to the 4mA current injection case but with reduced slope, i.e. reduced contrast. This aspect could be an important consideration in longitudinal studies where the change in conductivity in a tumor is investigated over time.

A simple setup was prepared where the separation between two closely separated nylon disks was used to assess resolution. It was found that the closest distance of 1mm was still detectable in those images. Construction of sophisticated high-resolution phantoms with agarose gel is a mechanically challenging task due to the lack of rigidity in the gel structure. Small structures easily melt and blend into each other making boundaries somewhat ambiguous. Although more complicated phantoms could be built with different materials to investigate the spatial resolution of the method, this simple phantom illustrates how well the separation between objects of different conductivity could be resolved.

Similarly, conductivity images collected from animals in vivo showed significantly increased conductivity in tumor areas. Tumor location was identified by contrast enhanced MRI. It is seen from these results that there is high correlation between the conductivity images and contrast enhanced MR images. Although they do not completely overlap, this is expected because the two

methods emphasize different properties of tumors. For example, edema will most likely show high conductivity but will not show signal enhancement with the CE-MRI. To exclude edematous regions from the conductivity images, one can use T2 weighted sequences that highlights edema. In this preliminary experiment, an animal with a large tumor size was imaged, which was available at the time. As seen in the CE-MRI images, the tumor had spread into several foci that encircled the animal's trunk. In large tumors, various compartments like edema, necrosis and viable tumor cells exist and their conductivity and contrast agent enhancement will be different. Currently, a longitudinal study is planned to observe changes in conductivity as well as Gd-DTPA based contrast enhancement in tumor structures as the tumor grows. The CE-MRI will be used to verify the MREIT results in vivo. At the end of the study, tumors will be excised and undergo histologic analysis. Contrast enhanced and T2 weighted images together with the MREIT maps will allow for the assessment of how conductivity correlates with different compartments in tumors. The positions and numbers of electrodes could be another factor that may confound the detection of some low conductivity structures close to surface. The effects of electrode placement will also be investigated in future studies.

In general, currents flowing in an object generate a 3D magnetic field. The currents flowing inside an imaging slice generate a magnetic field that has only a component, which is perpendicular to the plane of the slice. In this preliminary study, the magnetic fields generated by currents outside the imaging slice were ignored, reducing the reconstruction to 2D. Since most of the current flow will be concentrated between the electrodes, this approximation was deemed to be adequate for the pilot studies. 3D reconstruction methods may be developed that will account for such out-of-slice effects.

REFERENCES:

1. A. J. Surowiec, S. S. Stuchly, J. R. Barr, and A. Swarup, "Dielectric Properties of Breast Carcinoma and the Surrounding Tissues," *IEEE Trans. on BME, 35,* 257- 263, (1988).

2. J. G. Elmore, M. B. Barton, V. M. Moceri, S. Polk, P. J. Arena, and S. W. Fletcher, "Ten-year Risk of False Positive Screening Mammograms and Clinical Breast Examinations," *The New England Journal of Medicine, 338,* 1089-1096, (1998).

3. C. L. Christiansen, F. Wang, M. B. Barton, W. Kreuter, J. G. Elmore, A. E. Gelfand, and W. Fletcher, "Predicting the Cumulative Risk of False-Positive Mammograms," *Journal of the National Cancer Institute, 92,* 1657-1666, (2000).

4. J. G. Elmore, D. L. Miglioretti, L. M. Reisch, M. B. Barton, W. Kreuter, C. L. Christiansen, and S. W. Fletcher, "Screening Mammograms by Community Radiologists: Variability in False-Positive Rates," *Journal of the National Cancer Institute, 94,* 1373-1380, (2002).

5. S. K. Moore, "Better Breast Cancer Detection," *IEEE Spectrum, 38,* 50-54, (2001).

6. T. A. Coons, "MRI's Role in Assessing and Managing Breast Disease," *Radiological Technology, 67,* 311-336, (1996).

7. A. Malich, T. Boehm, M. Facius, M. G. Freesmeyer, M. Fleck, R. Anderson, and W. A. Kaiser, "Differentiation of Mammographically Suspicious Lesions: Evaluation of Breast Ultrasound, MRI Mammography and Electrical Impedance Scanning as Adjunctive Technologies in Breast Cancer Detection," *Clinical Radiolody, 56,* 278-283, (2001).

8. K. Boone, D. Barber, and B. Brown, "Imaging with Electricity: Report of the European Concerted Action on Impedance Tomography," *Journal of Medical Engineering and Technology, 21,* 201-232, (1997).

9. V. Cherepenin, A Karpov, A Korjenevsky, V. Kornienko, A. Mazaletskaya, D. Mazourov, and D Meister, "A 3D Electrical Impedance Tomography (EIT) System for Breast Cancer Detection," *Physiological Measurement, 22,* 9-18, (2001).

10. J. Estrela da Silva, J. P. Marques de Sá, and J. Jossinet, "Classification of Breast Tissue by Electrical Impedance Spectroscopy," *Medical and Biological Engineering and Computing*, *38*, 26-30, (2000).

11. A. Malich, T. Fritsch, R. Anderson, T. Boehm, M. G. Freesmeyer, M. Fleck, and W. A. Kaiser, "Electrical Impedance Scanning for Classifying Suspicious Breast Lesions: First Results," *Eur. Radiol.*, *10*, 1555-1561, (2000).

12. A. Malich, T. Fritsch, C. Mauch, T. Boehm, M. Freesmeyer, M. Fleck, R. Anderson, and W. A. Kaiser, "Electrical impedance scanning: A new technique in the diagnosis of lymph nodes in which malignancy suspected on ultrasound," *The British Journal of Radiology*, *74*, 42-47, (2001).

13. A. Malich, T. Boehm, M. Facius, M. Freessmeyer, M. Fleck, R. Anderson, and W. A. Kaiser, "Additional value of electrical impedance scanning: experience of 240 histologically-proven breast lesions," *European Journal of Cancer*, *37*, 2324-2330, (2001).

14. T. E. Kerner, K. D. Paulsen, A. Hartov, S. K. Soho, and S. P. Poplack, "Electrical Impedance Spectroscopy of the Breast: Clinical Imaging Results in 26 Subjects," *IEEE Trans. on Medical Imaging*, *21*, 638-645, (2002).

15. M. Assenheimer, O. Laver-Mokovitz, D. Malonek, D. Manor, U. Nahaliel, R. Nitzan, and A. Saad, "The T-SCAN™ technology: electrical impedance as a diagnostic tool for breast cancer detection," *Physiological Measurement*, *22*, 1-8, (2001).

16. Y. Z. Ider and O. Birgul, "Use of the magnetic field generated by the internal distribution of injected currents for Electrical Impedance Tomography (MR-EIT)," *Elektrik, Turkish Journal of Electrical Engineering and Computer Sciences, 6*, 215-225, (1998).

17. O. Birgul, M Eyuboglu, and Y. Z. Ider, "A New Technique for High Resolution Absolute Conductivity Imaging Using Magnetic Resonance-Electrical Impedance Tomography (MR-EIT)," *Proceedings of SPIE - the International Society for Optical Engineering, Medical Imaging, 4320*, 880-888, (2001).

18. H. S. Khang, B. I. Lee, S. H. Oh, E. J. Woo, S. Y. Lee, M. H. Cho, O. Kwon, J. R. Yoon, and J. K. Seo, "J-Substitution Algorithm in Magnetic Resonance Electrical Impedance

Tomography (MREIT): Phantom Experiment for Static Resistivity Images," *IEEE Trans. on Medical Imaging, 21*, 695-702, (2002).

19. O. Birgul, B. M. Eyuboglu, and Y. Z. Ider, "Current constrained voltage scaled reconstruction (CCVSR) algorithm for MR-EIT and its performance with different probing current patterns," *Physics in Medicine and Biology, 48*, 653-671, (2003).

20. O. Birgul, B. M. Eyuboglu, and Y. Z. Ider, "Experimental results for 2D magnetic resonance–electrical impedance tomography (MR-EIT) using magnetic flux density in one direction," *Physics in Medicine and Biology, 48*, 3485-3504, (2003).

21. S. H. Oh, J. Y. Han, S. Y. Lee, M. H. Cho, B. I. Lee, and E. J. Woo, "Electrical Conductivity Imaging by Magnetic Resonance Electrical Impedance Tomography (MREIT)," *Magnetic Resonance in Medicine, 50*, 875-878, (2003).

22. G. C. Scott, M. L. G. Joy, R. L. Armstrong, and R. M Hankelman, "Measurement of Non-uniform Current Density by Magnetic Resonance," *IEEE Trans on Medical Imaging, 10*, 362-374, (1991).

23. Y. Z. Ider and L. M. Muftuler "Measurement of AC Magnetic Field Distribution using Magnetic Resonance Imaging," *IEEE Trans. on Medical Imaging, 16*, 617-622, (1997).

24. U. Mikac, F. Demsar, K. Beravs, and I. Sersa, "Magnetic Resonance Imaging of Alternating Electric Currents," *Magnetic Resonance Imaging, 19*, 845-856, (2001) .

25. G. C. Scott, M. L. G. Joy, R. L. Armstrong, and R. M. Hankelman, "Electromagnetic Considerations for RF Current Density Imaging," *IEEE Trans. on Medical Imaging, 14*, 515-524, (1995).

26. Y.A. Glickman, O. Filo, U. Nachaliel, S. Lenington, S. Amin-Spector, R. Ginor, "Novel EIS Postprocessing Algorithm for Breast Cancer Diagnosis", *IEEE Trans. on Medical Imaging, 21*, 710-712, (2002).

27. Ider YZ, Eyuboglu BM, Kuzuoglu M, Leblebicioglu K, Baysal U, Caglar BK, Birgul O, "A method for comparative evaluation of EIT algorithms using a standard data set", *Physiol. Meas., 16*, A227-A236, (1995).

Table.I. Mean and standard deviation of relative conductivity (σ_{ir}, σ_{or}) values in contrast phantoms calculated by the MREIT method. Results are reported for both injected current amplitudes.

Figure.1. Timing diagram of the pulse sequence used in the MREIT experiments.

Figure.2. Schematic of the experimental setup. AH is the animal holder, which is placed inside the MRI RF coil.

Figure.3.a. Spin-Echo image of 1/4 contrast phantom. The higher conductivity region is marked with red dashed lines and it is barely distinguishable in the MR image.

Figure.3.b. Conductivity images of 1/10 contrast (top row) and 1/4 contrast (bottom row) with 2mA and 4mA current injection cases

Figure 3.c. The plots of relative conductivity changes in the object versus relative conductivity values obtained from MREIT images. Plots are given for both of the injected current amplitudes. Error bars are also included in these plots.

Figure.4.a. Conductivity images of resolution phantom with 2mA and 4mA current injection cases. Small dark circular areas show high conductivity compartments (insulating disks)
Fig.4.b. A profile taken diagonally from the conductivity image of resolution phantom going through the centers of the small disks. This profile is given for the 4mA current injection case.

Figure.5. Axial slices from an SD rat inoculated with a R3230 AC tumor showing: (a) Conductivity; (b) CE-MRI; and (c) spatial correlation of CE-MRI and MREIT. The tumor had spread to multiple foci surrounding the body. In (a), red shows high conductivity and blue shows low conductivity regions; whereas red regions in (b) shows enhancement by Gd-DTPA; Areas that have both high conductivity and also enhanced by contrast agent are shown in hot colors in (c).

Figure.5.d. FEM mesh constructed from the anatomical MR Image

	$\sigma_o/\sigma_i = 1/4$ phantom (m±std)		$\sigma_o/\sigma_i = 1/10$ phantom (m±std)	
	I=2mA	I=4mA	I=2mA	I=4mA
Inside small disk (σ_{ir})	235.4±10.5	229.6±18.4	233.4±15.4	226.6±21.2
Background (σ_{or})	81.2±18.3	63.8±14.7	50.1±17.9	36.1±12.3

Table I
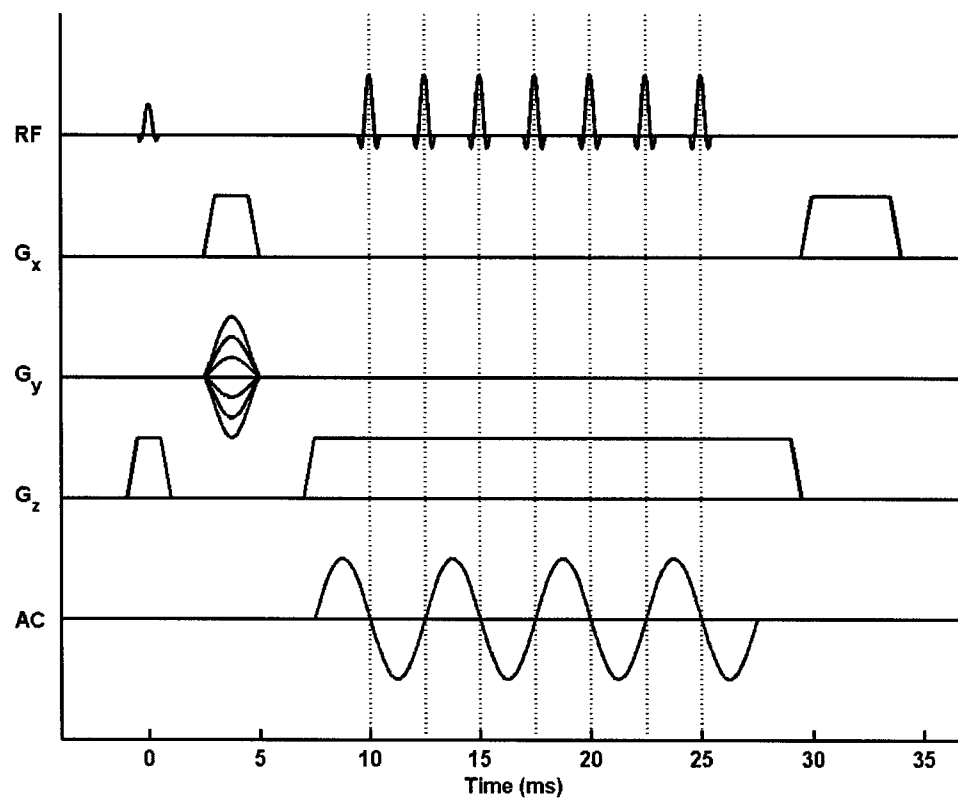
Fig.1.

Fig.2
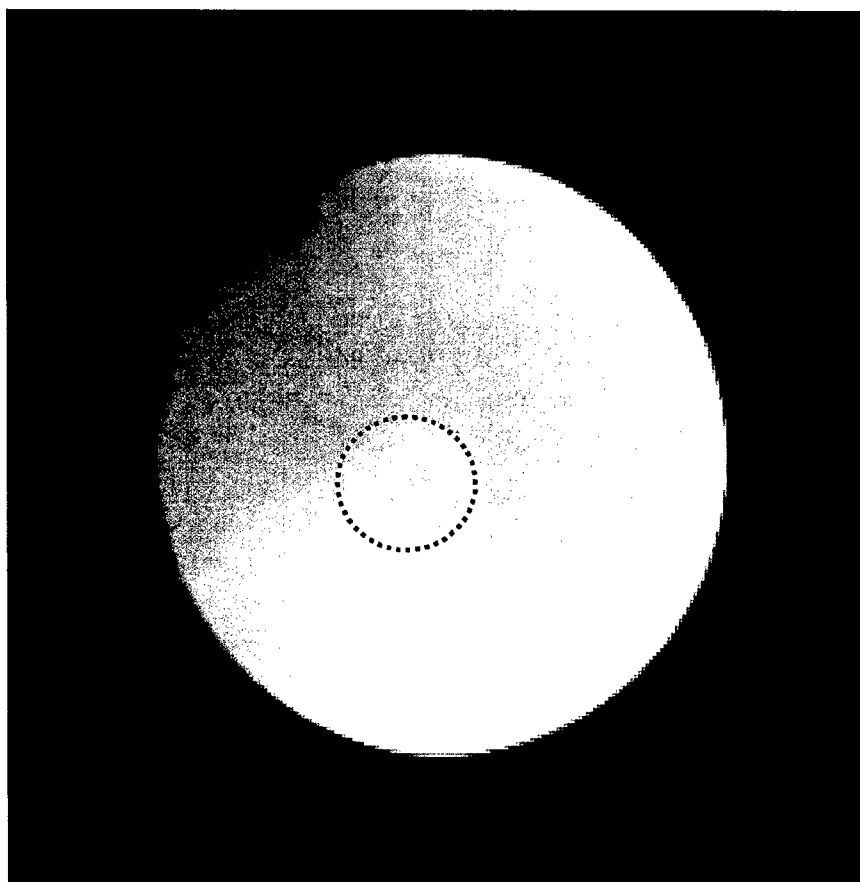
Fig.3.a.

10 to 1 : 2mA   **10 to 1 : 4mA**
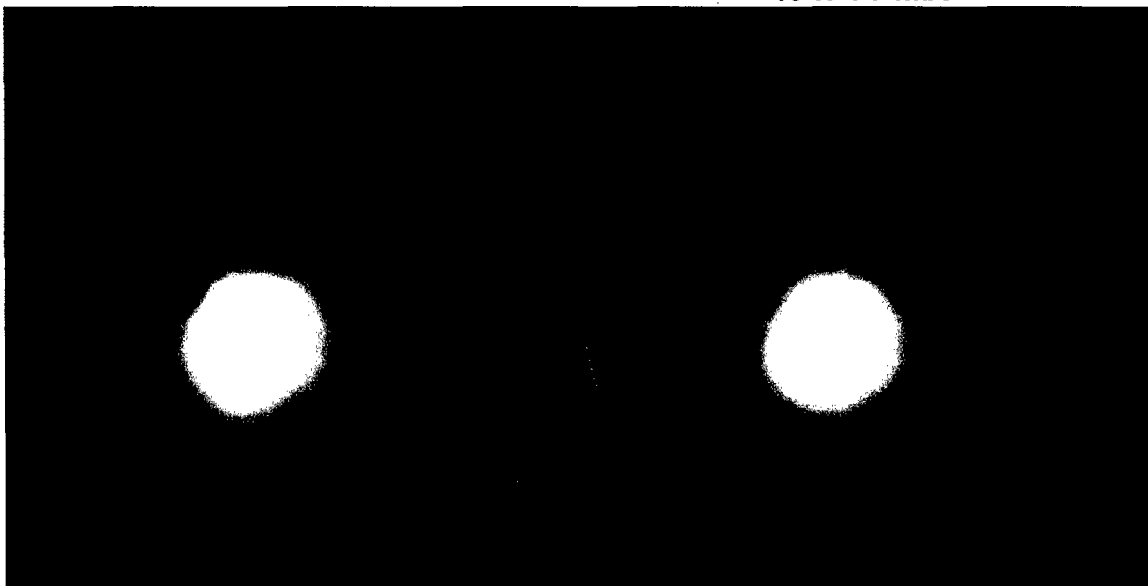
4 to 1 : 2mA   **4 to 1 : 4mA**

Fig.3.b.
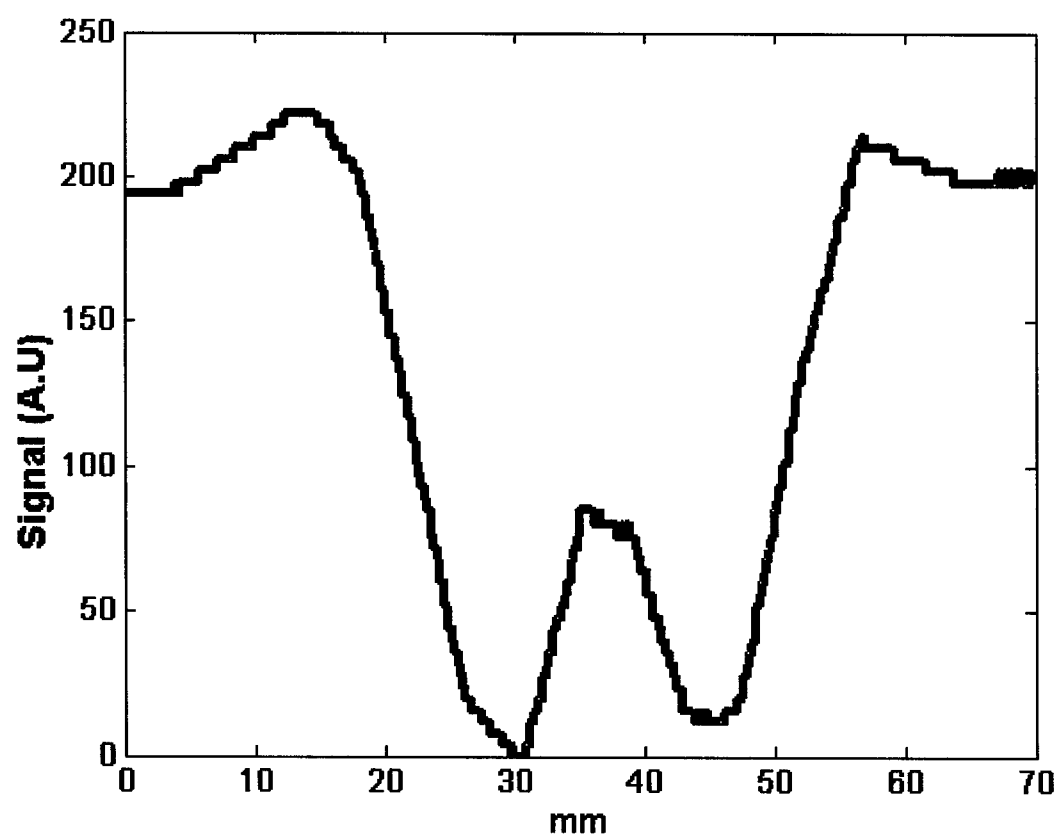
Figure 3.c.

resolution : 2mA   **resolution : 4mA**
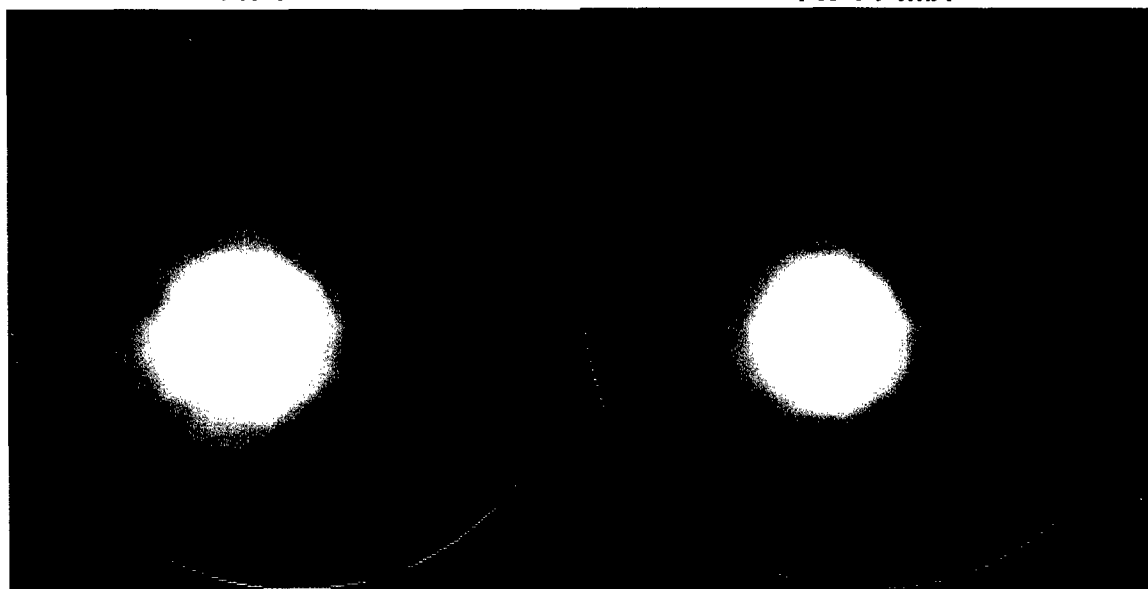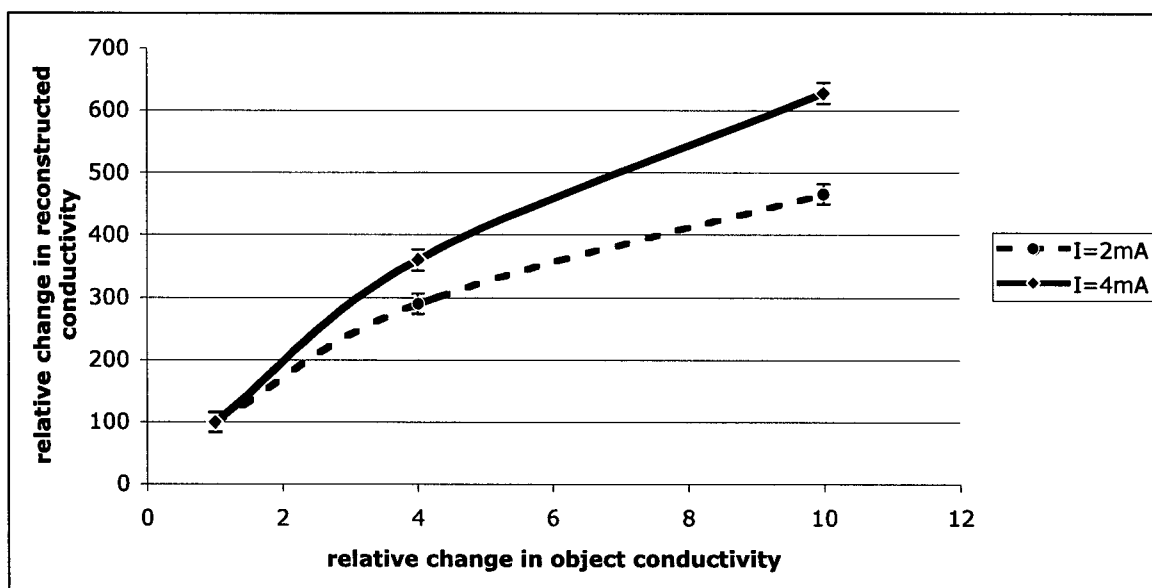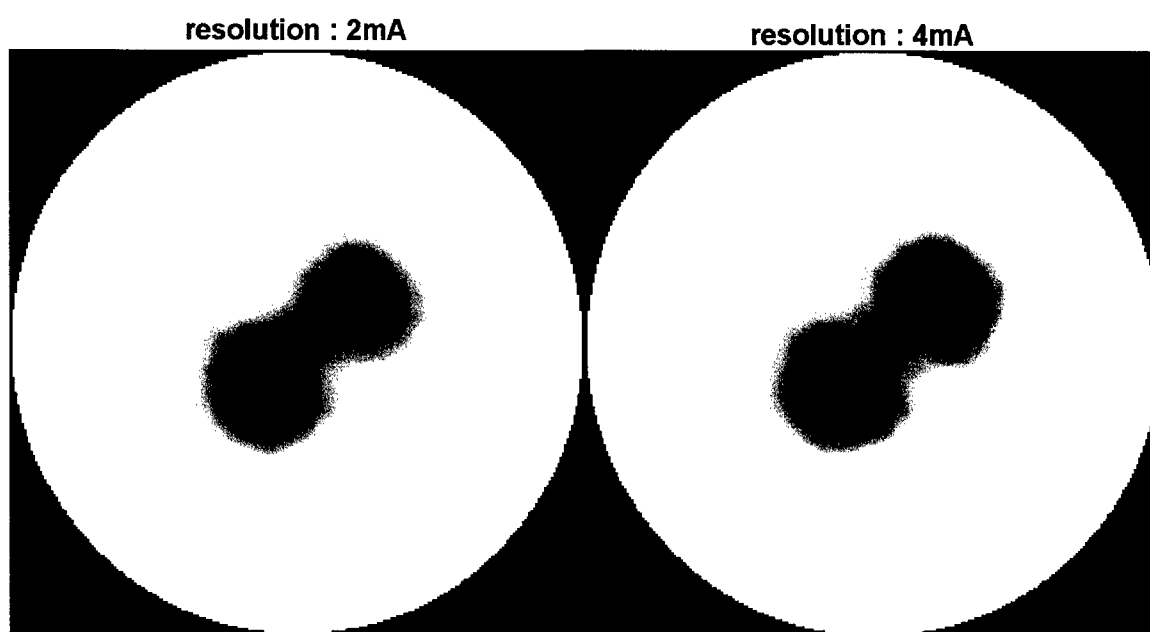
Fig.4.a.

Fig.4.b.

Fig.5.a, b, c

Fig.5.d.